JGR Oceans

RESEARCH ARTICLE
10.1029/2021JC017375

Key Points:

- Pairs of surface drifters and RAFOS floats drifting at 300 and 1,500 dbar were released simultaneously in the Gulf of Mexico between 2016 and 2018
- Relative diffusivity at 300 and 1,500 dbar is on average 2 and 5 times weaker than at the surface, respectively
- Topography and sheared boundary currents might play a major role in float dispersion

Correspondence to:
T. Meunier,
tmeunier@whoi.edu

Citation:
Meunier, T., Pérez Brunius, P., Rodríguez Outerelo, J., García Carrillo, P., Ronquillo, A., Furey, H., et al. (2021). A Deep Water Dispersion Experiment in the Gulf of Mexico. *Journal of Geophysical Research: Oceans*, *126*, e2021JC017375. https://doi.org/10.1029/2021JC017375

Received 22 MAR 2021
Accepted 16 SEP 2021

A Deep Water Dispersion Experiment in the Gulf of Mexico

Thomas Meunier[1], Paula Pérez Brunius[2], Javier Rodríguez Outerelo[2], Paula García Carrillo[2], Argelia Ronquillo[2], Heather Furey[1], Andrée Ramsey[1], and Amy Bower[1]

[1]Physical Oceanography Department, Woods Hole Oceanographic Institution, Woods Hole, MA, USA, [2]Departamento de Oceanografía, Centro de Investíagacion Cientifica y de Educación Superior de Ensenada, Ensenada, B.C., Mexico

Abstract The Deep Water Horizon oil spill dramatically impacted the Gulf of Mexico from the seafloor to the surface. While dispersion of contaminants at the surface has been extensively studied, little is known about deep water dispersion properties. This study describes the results of the Deep Water Dispersion Experiment (DWDE), which consisted of the release of surface drifters and acoustically tracked RAFOS floats drifting at 300 and 1,500 dbar in the Gulf of Mexico. We show that surface diffusivity is elevated and decreases with depth: on average, diffusivity at 1,500 dbar is 5 times smaller than at the surface, suggesting that the dispersion of contaminants at depth is a significantly slower process than at the surface. This study also examines the turbulent regimes driving the dispersion, although conflicting evidences and large uncertainties do not allow definitive conclusions. At all depths, while the growth of dispersion and kurtosis with time supports the possibility of an exponential regime at very short time scales, indicating that early dispersion is nonlocal, finite size Lyapunov exponents support the hypothesis of local dispersion, suggesting that eddies of size comparable to the initial separation (6 km), may dominate the early dispersion. At longer time scales, the quadratic growth of dispersion is indicative of a ballistic regime, where a mean shear flow would be the dominating process. Examination of the along- and across-bathymetry components of float velocities supports the idea that boundary currents could be the source for this shear dispersion.

Plain Language Summary The 2010 Deep Water Horizon oil spill has dramatically impacted the Gulf of Mexico's marine environment from the seafloor to the surface. While dispersion of contaminants at the surface has been extensively studied over the past decades, little is known about the deep water dispersion properties of the ocean, and the fate of deep contaminants is uncertain. This paper describes the results of the Deep Water Dispersion Experiment that took place in the western Gulf of Mexico, a deep water drilling operation area. The experiment consisted in the simultaneous release of surface drifters and floats drifting at 300 and 1,500 m, to assess the variations of dispersion properties with depth for the first time. It is shown that diffusivity is weaker in depth that at the surface, so that contaminants would spread less rapidly.

1. Introduction

At scales larger than a few kilometers, the ocean motion is essentially horizontal, and the fate of tracers is primarily determined by lateral stirring (horizontal at the surface and isopycnal at depth) by eddies. Despite the baroclinicity of the oceanic currents and eddies, most concepts from the 2D turbulence theory were shown to largely apply to geostrophic turbulence (Charney, 1971; McWilliams, 1989; Rhines, 1979), and the theory of particle dispersion in 2D turbulent flows has provided a solid background for the study of passive tracer evolution in the ocean (Babiano et al., 1990; Batchelor, 1952; Bennett, 1987; Kraichnan, 1967; LaCasce, 2008; Lin, 1972; Lundgren, 1981). Lagrangian experiments, involving the release of large numbers of satellite-tracked drifting buoys in pairs or triplets, and studying their relative movement as turbulent advection separates them, have successfully applied these concepts to reveal the turbulent regimes occurring over a variety of time and space scales in the ocean (Colin de Verdiere, 1983; Davis, 1991; LaCasce & Ohlmann, 2003; Ollitrault et al., 2005; Zavala Sansón, 2015, among many).

Particles in the ocean are subject to chaotic advection by eddies that have a broad range of scales, from a few kilometers to several hundreds, and their relative contribution to the turbulent kinetic energy (KE) decreases with decreasing length scale, resulting in the typical negative slope of KE spectra. However, depending on regional processes, eddies may be shed with a preferential length scale. For instance, baroclinically unstable oceanic currents tend to shed eddies with radii that are close to the local first Rossby radius. At scales that are larger than this energy-injection scale, the KE spectrum slopes as $k^{-5/3}$ (where k is the wavenumber) as energy is transferred from the injection scale toward larger scales. At scales that are smaller than the injection scale, the KE spectrum's slope becomes steeper than k^{-3} and enstrophy is transferred toward smaller scales. The rate at which two particles separate entirely depends on the velocity difference at each particle's location. The scale dependence of this velocity difference is quantified by the KE spectrum, so that pair dispersion statistics can provide useful information on the latter.

When the separation of a particle pair is primarily driven by eddies that are much larger than the pair separation, dispersion is called nonlocal, while when it is driven by eddies whose size is comparable with the pair separation, dispersion is called local. The transition between these two regimes occurs at the energy-injection scale, and, as will be recalled below, relative dispersion experiments provide crucial information on the turbulent regimes that could not be inferred otherwise.

Beyond the fundamental goal of better understanding the nature of oceanic turbulence, the study of relative dispersion has direct applications in a number of essential biological, environmental, and economical issues, from the distribution of plankton patches (Bennett & Denman, 1985), the dispersal of fish larvae (Mariani et al., 2007), the fate of plastic waste in the ocean (van Sebille et al., 2012), and the evolution of contaminant spills (North et al., 2011). While most of these problems are confined to the surface mixed layer, the recent Deep Water Horizon catastrophe in the Gulf of Mexico (GoM), discharging 650,000 m^3 of oil at a depth of 1,200 m (Kujawinski et al., 2011; McNutt et al., 2012), showed the necessity of understanding dispersion properties of the full water column: oil is composed of a variety of constituents evolving into droplets of different sizes (Reddy et al., 2012), each reaching a different neutral buoyancy depth before dispersing, and resulting in a series of distinct plumes from the sea-floor to the surface (North et al., 2011). The development of deep sea mining, involving the injection of contaminants and sediments throughout the water column, has also highlighted the necessity of an in-depth assessment of the deep and intermediate dispersion properties of the ocean (Drazen et al., 2020).

Thanks to the early work of LaCasce and Ohlmann (2003), and the extensive Lagrangian experiments carried out after the Deep Water Horizon spill, such as the Grand Lagrangian Deployment (GLAD; Beron-Vera & LaCasce, 2016; Poje et al., 2014, 2017), surface dispersion properties of the northern and western GoM are well documented. While the latter was shown to be local at scales of O(10–100 km) (Richardson regime), its small time and spatial scale behavior are more ambiguous. LaCasce and Ohlmann (2003) and Beron-Vera and LaCasce (2016) reported nonlocal dispersion (so called exponential or Lundgren regime) at times shorter than a few days and separations smaller than the first Rossby radius (≈50 km in the GoM), while Poje et al. (2014) found a Richardson regime down to the smallest resolved scales (≈1 km), consistent with local dispersion by energetic submesoscale structures. At these scales, Balwada, LaCasce, et al. (2016) showed that dispersion was driven by divergent motion while rotational motion is responsible for the larger scale dispersion.

Despite this exceptional Lagrangian sampling effort in the surface GoM, direct observations of relative dispersion at depth are lacking. More generally, observations of deep ocean dispersion are rare. Notable exceptions include the work of Zhang et al. (2001) and LaCasce and Bower (2000) who studied the dispersion of RAFOS and SOFAR floats drifting between 400 and 1,300 dbar in the North Atlantic and Ollitrault et al. (2005) who used 700 dbar SOFAR floats in the same oceanic basin. While all clearly identified a Richardson regime at scales ranging between 40 and 300 km, the existence of an exponential regime at small scale at these depths remained uncertain, possibly due to the relatively large initial separations of float pairs. Deep lateral diffusivity was also estimated by LaCasce et al. (2014) using isopycnal RAFOS floats in the Antarctic Circumpolar Current. Using a numerical model validated from the RAFOS observations at ≈1,000 m depth, they showed that mixing was maximum at depths between 1,500 and 2,000 m.

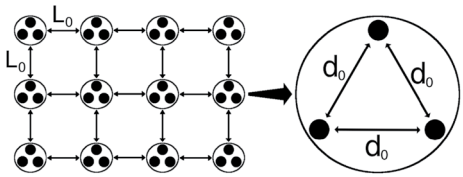

Figure 1. Float launch strategy: triplets are launched following a regular array and are separated by a distance $L_0 \approx 50$ km. Within each triplet, floats are launched with an initial separation of $d_0 \approx 100$ m. The initial separation considered in this work is however of $d_0 = 6$ km, because of the uncertainty of the RAFOS positioning.

As part of the Gulf of Mexico Research Consortium (CIGoM) project—a large community effort funded by the Mexican Government to better understand the dynamics of the GoM and its response to oil spills, the Deep Water Dispersion Experiment (DWDE) was designed to simultaneously measure the deep, intermediate, and surface dispersion properties of the Perdido region in the western GoM. The Perdido region, located across Mexico and USA's exclusive economic zones, is a particularly critical region, as it shelters some of the world's deepest drilling operations, at about 200 miles from the Texas and Tamaulipas shores. The experiment, performed in four legs between June 2016 and November 2018, consisted of the simultaneous release of surface drifters and RAFOS floats drifting at 300 and 1,500 dbar, to assess and compare the water column's dispersion properties. To our knowledge, this is only the second experiment of simultaneous release of drifting instruments at different depths, after Balwada et al. (2021)'s study of the deep dispersion at two different depth ranges in the Antarctic Circumpolar Current, a strong zonal current suppressing eddy dispersion in the upper layer. Beyond the essential environmental necessity of studying deep dispersion in the western GoM, the DWDE also provides one of the first direct observations of the depth dependence of dispersion and diffusivity.

2. Data and Methods

2.1. Data

The deployment strategy was designed to answer Beron-Vera and LaCasce (2016)'s concerns on the biasing effect of releasing simultaneously all pairs in the same location. To avoid undesired correlation between different pairs, instruments were released as triplets (each triplet yielding three pairs) approximately 50 km apart (the average first baroclinic Rossby radius in the GoM) in the cross-slope direction, during four release campaigns, 6 months apart, between June 2016 and December 2018. Individual floats within a triplet had an initial separation of 100 m. The survey strategy is summarized in Figure 1, while the deployment site is shown in Figures 2c–2e. From a total of 84 RAFOS floats whose data were recovered (44 at 300 dbar and 40 at 1,500 dbar), 51 completed a full mission, while 33 surfaced earlier, most likely due to attacks by large pelagic fish. These early risers were almost entirely 300 dbar floats, resulting in an incomplete data set and weaker statistical significance of the results at this depth. The history of the number of successful floats collecting data simultaneously in the water is shown in Figure 3d. While pairs were originally separated by approximately 100 m, we chose a larger value of 6 km as the initial separation, because of the uncertainty on the relative position of RAFOS floats (≈1 km). The data set used in the present study is composed of 207 original pairs of surface drifters, 37 pairs of 300 dbar RAFOS floats, and 40 pairs of 1,500 dbar RAFOS floats (Table 1). We also included chance pairs, which are floats that were not initially launched together, but approached one another by chance (LaCasce & Ohlmann, 2003; Morel & Larceveque, 1974), resulting in a total number of 294, 39, and 43 pairs for the surface, 300, and 1,500 dbar data sets, respectively. The repeated occurrence of early surfacing 300 dbar floats results in shorter time series at this depth and limits our analysis to the first 100 days (Figures 3f and 3h). The sampling rate was of 1 h for surface drifters and 8 h for RAFOS floats. Although the original sampling rate of surface drifters is primarily used in this study, all variables were also computed using a degraded rate, subsampled to the RAFOS floats 8 h rate, as an indication that inconsistency of sampling rates does not bias the results.

The ballast depths of the RAFOS floats were chosen to represent the top and deep layers of the GoM, whose circulation is essentially two-layered (Hamilton et al., 2018). Note that the surface drifters are drogued at 1 dbar, so that their drift and dispersion are also directly influenced by surface processes such as Stokes drift, Ekman drift, or Langmuir circulations, while the 300 and 1,500 dbar are expected to primarily be subject to geostrophic turbulent dispersion. RAFOS floats positions were calculated using an array of five sound sources deployed prior to the experiments (Figure 2).

While the number of RAFOS pairs is small compared to typical surface drifter experiments, yielding a higher level of uncertainty, it should be mentioned that deep dispersion experiments are rare and any new information is valuable.

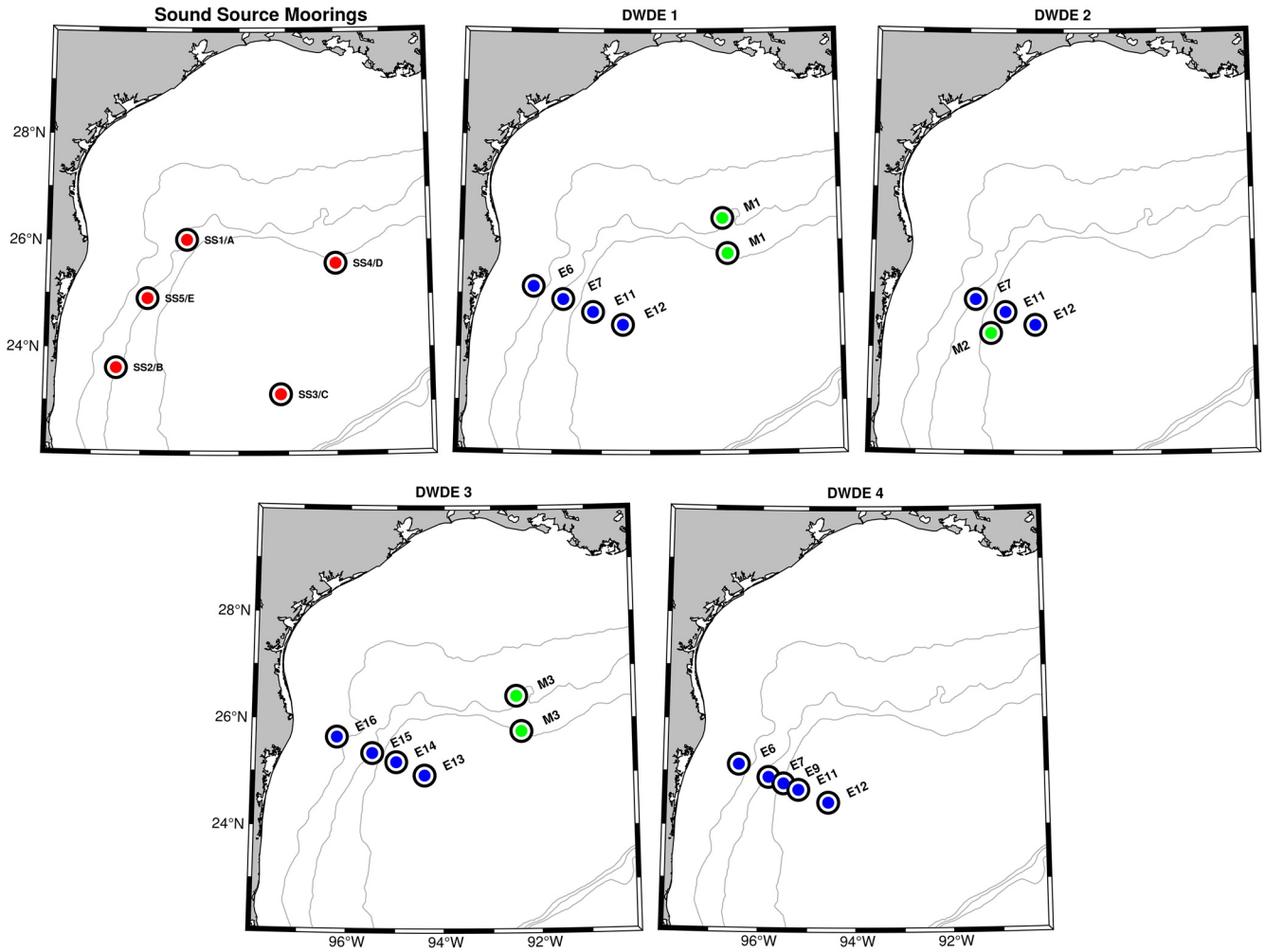

Figure 2. Float launch location. The sound sources are represented by red dots in panel (a), while the launching sites for the four experiments are shown as blue dots in panels (b–e).

To describe the general context in which floats drift, we also used gridded fields of the mean surface and deep (1,500–2,500 m) circulations. The surface circulation product used is GulfFlow, a 1/4° climatology based on 3,761 drifter trajectories in the GoM (Lilly & Pérez-Brunius, 2021), while the deep circulation product is Pérez-Brunius et al. (2018)'s mean velocity field computed from 152 RAFOS floats drifting between 1,500 and 2,500 m in the GoM.

2.2. Theoretical Background

Important theoretical efforts in Lagrangian fluid dynamics since the early fifties (e.g., Artale et al., 1997; Babiano et al., 1990; Batchelor, 1952; Bennett, 1987; Lundgren, 1981) provided an arsenal of diagnostic tools that allow us to discriminate between turbulent regimes. A comprehensive examination of the variables used in the present study was discussed in a number of reviews (e.g., Davis, 1991; LaCasce, 2008); their definitions and properties are only briefly presented below.

The separation vector $\vec{D}$ between two particles whose Lagrangian coordinates at time t are $\vec{a}_1$ and $\vec{a}_2$ is defined as

$$\vec{D}(t,\vec{D}_0) = \vec{D}_0 + \vec{A}(\vec{a}_1,t) - \vec{A}(\vec{a}_2,t), \quad (1)$$

where $\vec{D}_0$ is the initial separation vector, and $\vec{A}(\vec{a}_i,t)$ is the absolute displacement vector of particle i at time t. In this work, initial separation is chosen to be 6 km. Relative dispersion is defined as the ensemble mean at

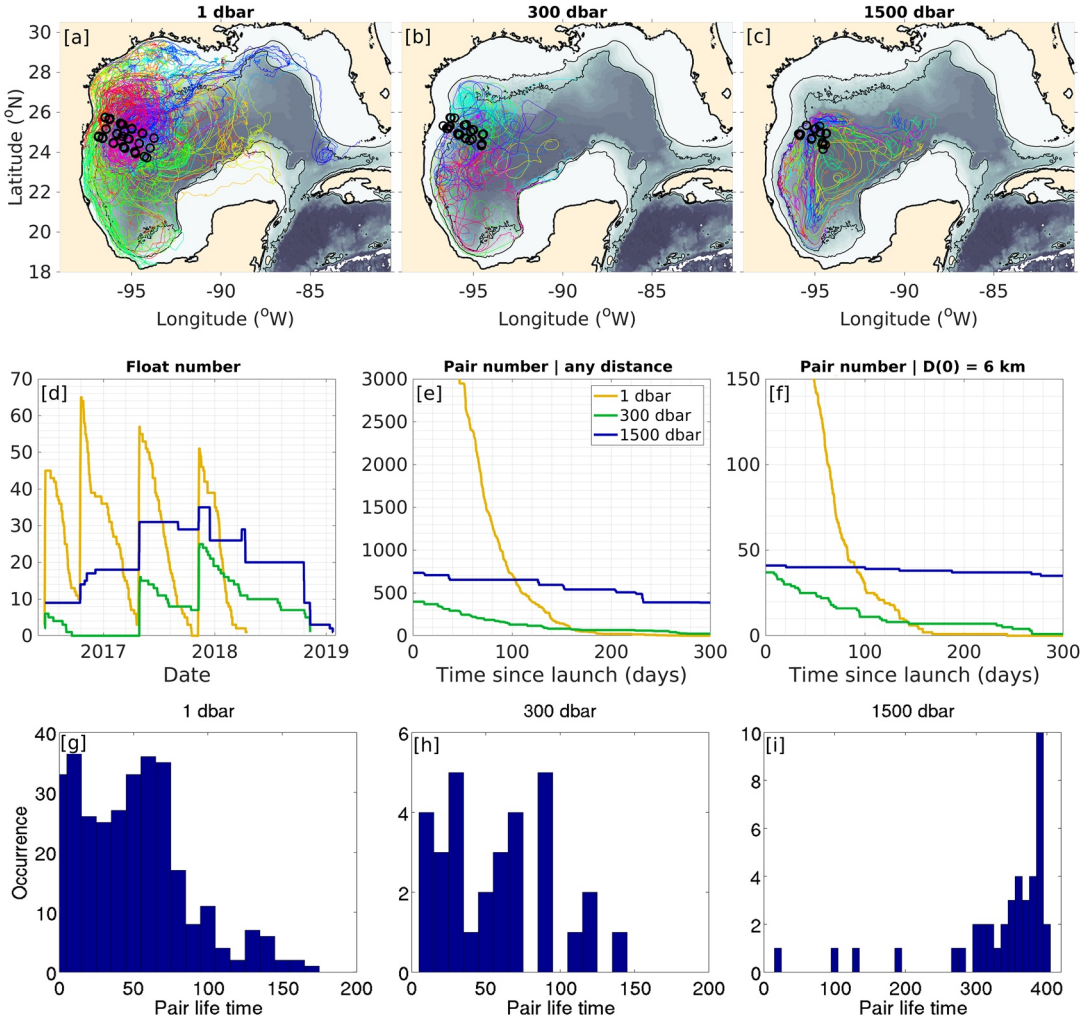

Figure 3. (a) Spaghetti plot of the surface drifters trajectories during the whole experiment. The black circles represent the launch locations. (b) Same as (a) for the 300 dbar RAFOS floats. (c) Same as (a) for the 1,500 dbar RAFOS floats. (d) Time series of the total number of drifters and floats in the water. The yellow line represents the surface drifters, while the green and blue lines represent the 300 and 1,500 dbar RAFOS floats, respectively. (e) Total number of pairs regardless of the initial separation at each depth. (f) Total number of pairs with an initial separation of 6 ± 1 km. (g) Histogram of the surface drifters lifetimes. (h) Same as (g) for the 300 dbar floats. (i) Same as (g) for the 1,500 dbar floats.

Table 1
Characteristics of the Float Clusters at All Depths

	1 dbar	300 dbar	1,500 dbar
Initial float number	207	44	40
Number after 50 days	148	31	40
Number after 100 days	64	20	40
Median life time (days)	74	106	540
Initial pair number (D_0 = 6 km)	294	39	43
Number after 50 days	136	25	42
Number after 100 days	29	12	41
Median life time (days)	47	67	367

time t of the squared norm of the separation vectors of all particle pairs that were originally separated by a distance $D_0 = \|\vec{D}_0\|$:

$$D^2(t, D_0) = \langle \vec{D}(t, \vec{D}_0) \cdot \vec{D}(t, \vec{D}_0) \rangle. \quad (2)$$

Considering a tracer patch as a large number of individual particles, relative dispersion can be thought of as a proxy of the instantaneous area of a patch whose initial area was D_0^2. Relative diffusivity is a measure of the rate of change of this area with time, or spreading, and is defined as

$$K(t, D_0) = \frac{1}{2}\frac{d}{dt} D^2(t, D_0). \quad (3)$$

Relative diffusivity is a scale-dependent variable, and the relationship between $K(t, D_0)$ and the separation scale $\|\vec{D}(t)\|$ is an important indicator of the turbulent regime and the energy dissipation rate. In the Richardson's regime, where dispersion is driven by eddies that are the same scale as pair separation (local regime), diffusivity is expected to grow as

$K(D) \propto \epsilon^{1/3} D^{4/3}$ (Batchelor, 1952; LaCasce, 2008), where ϵ is the energy dissipation rate. In the exponential regime (also known as Lundgren or Lin regime), where dispersion is driven by eddies that are larger than pair separation (nonlocal regime), diffusivity is expected to grow as $K(D) \propto D^2$ (Beron-Vera & LaCasce, 2016; Lin, 1972; Lundgren, 1981). These different regimes are directly linked to the Eulerian KE spectrum: the Richardson regime is found at scales larger than the energy-containing eddies, where energy cascades toward larger scales and the KE spectrum slopes as $k^{-5/3}$, while the exponential regime is expected at scales that are smaller than the energy-containing eddies, which corresponds to a direct enstrophy cascade and a KE spectrum that is steeper than k^{-3} (Kraichnan, 1967). Similarly, the time dependence of dispersion provides information on the turbulent regime and the energy or enstrophy dissipation rates, with typical growth laws of $D^2 \propto \epsilon t^3$ and $D^2 \propto e^{c\eta^{1/3}\gamma t}$ (where γ is the exponential growth rate, η is the enstrophy dissipation rate, and c is a constant) for the local and nonlocal regimes, respectively (LaCasce, 2008).

When using a limited number of particle pairs (as is the case in the DWDE), or sampling regions of the ocean where the 2D turbulence theory's hypothesis (stationary and isotropic turbulence in an infinite domain) does not hold, as is the case for the semienclosed GoM, the fundamental relations between dispersion and time, or between relative diffusivity and separation, can eventually be uncertain or contradictory (Artale et al., 1997; Beron-Vera & LaCasce, 2016; LaCasce, 2008). A number of Lagrangian diagnostic tools can then help to distinguish between the possible regimes.

In particular, we will make use of the finite size Lyapunov exponent (FSLE; Artale et al., 1997; Aurell et al., 1996; LaCasce & Ohlmann, 2003), which is a measure of the (inverse) average time necessary for pair separation to increase by a chosen factor α (set to $\sqrt{2}$ here). The computation procedure consists of selecting a series of pair separation distances D_i growing geometrically as $D_{i+1} = \alpha D_i$, and averaging the inverse of the finite time T_i necessary for separation distance to grow from D_i to D_{i+1}. The FSLE is then defined as

$$\lambda = ln(\alpha)\langle\frac{1}{T_i}\rangle, \tag{4}$$

where the ensemble averaging is performed on each separation distance D_i. To detect successive crossings at the smallest resolved spatial scales, time series of separation were first linearly interpolated to a finer time step (one 96th of a day). Because FSLEs are defined in terms of spatial rather than temporal scales, they are particularly suited for the study of dispersion in closed basins where the size of the eddies is not very small compared to the size of the domain (Artale et al., 1997). Also, FSLE does not depend on the initial separation $\vec{D}_0$, so that one can use all available pairs for a given separation scale, regardless of the initial conditions (LaCasce, 2008). In the Richardson's regime, FSLE decays as $\lambda \propto D^{-2/3}$, while it is constant in the exponential regime ($\lambda \propto D^0$; Balwada et al., 2021; LaCasce & Ohlmann, 2003).

The kurtosis of the pair separation probability density function (PDF) will also be discussed. It is the PDF's fourth moment and is a measure of the flatness of the distribution (LaCasce, 2008; LaCasce & Bower, 2000; LaCasce & Ohlmann, 2003), defined as

$$Ku(t) = \frac{\langle\|\vec{D}\|^4\rangle}{\langle\|\vec{D}\|^2\rangle^2}. \tag{5}$$

In Richardson's regime, kurtosis has a constant value of 5.6, while it grows exponentially in the exponential regime (Beron-Vera & LaCasce, 2016; LaCasce, 2008).

Finally, note that the exponential and Richardson regimes occur at finite time, when the particles are close enough so that their absolute velocities are still correlated. A third case, the Rayleigh regime, is found in the long-time asymptotic limit, as the particles separation becomes large compared to the eddies size. In that regime, while the Eulerian KE spectrum's slope remains similar to the Richardson's regime ($k^{-5/3}$), the growth of relative dispersion becomes linear, while relative diffusivity saturates at a constant value, corresponding to twice the single-particle (or absolute) diffusivity (Babiano et al., 1990).

Uncertainties were computed for all variables using the Bootstrap method, which consists in generating a number of subsamples by randomly picking pairs from the original data set. The number of subsamples used here is 1,000. The error bars included in the figures represent the 95% confidence interval, that is, the range of values containing 95% of the mean values obtained from the 1,000 subsamples.

2.3. Topographic Projections

In order to study the impacts of topography on float trajectories and pair separation, the local along- and across-bathymetry components of the velocity vectors were computed for each displacement. The projection was performed using NOAA's ETOPO-1 1° gridded bathymetry (Amante & Eakins, 2009), smoothed using a 2D Gaussian filter with isotropic decorrelation radii of 50 km. The along- and across-bathymetry components are computed from the water depth gradient at the position of the float, following LaCasce and Speer (1999):

$$u_l(x,y,t) = \vec{k} \cdot \vec{u}(x,y,t) \times \frac{\vec{\nabla} H(x,y)}{|\vec{\nabla} H(x,y)|}, \tag{6}$$

$$u_c(x,y,t) = \vec{u}(x,y,t) \cdot \frac{\vec{\nabla} H(x,y)}{|\vec{\nabla} H(x,y)|}, \tag{7}$$

where u_l and u_c are the along- and across-bathymetry components of the velocity vector, respectively, H is the local water depth, $\vec{k}$ is the vertical unit vector, and $\vec{u}$ is either the float velocity or the pair separation velocity, depending if we focus on absolute or relative displacements. A good indicator of topographic anisotropy is the ratio of the mean along- and across-bathymetry components of the absolute and relative velocity ($\mathcal{R}_a$ and $\mathcal{R}_r$):

$$\mathcal{R} = \frac{\langle |u_l| \rangle}{\langle |u_c| \rangle}, \tag{8}$$

where $\langle \cdot \rangle$ is the ensemble averaging operator, and u_l and u_c are either the components of the absolute velocity or of the relative (pair separation) velocity.

3. Results

Trajectories of all surface drifters, 300, and 1,500 dbar RAFOS floats are shown in the spaghetti plots of Figures 3a–3c, respectively. The western GoM was densely sampled at all depths. Surface drifters and 1,500 dbar floats traveled eastward as far as 88°W (eastward of 88°W in the case of outliers), while the 300 dbar floats remained west of 90°W probably because of their average shorter trajectories. At all depths, the westward spreading of the floats is blocked by the topography. Some float trajectories are reminiscent of the dominating patterns of the mean western GoM circulations from Lilly and Pérez-Brunius (2021) and Pérez-Brunius et al. (2018) (Figure 5): at the surface, drifters circle around the Campeche gyre in the south-western corner, while at 1,500 dbar, RAFOS floats closely follow the south-western boundary current and circle around the Sigsbee abyssal gyre.

A more detailed time evolution of the float displacements is shown in Figure 4, where the daily position of each float is color coded. Some clear along-shore trajectories are evident as the westernmost drifters reach the continental shelf and slope. After 10 days, the average distance traveled is of 210, 170, and 90 km for the 1, 300, and 1,500 dbar floats, respectively. After 50 days, two surface drifters have traveled over 700 km eastward and reached 88°W, while four have reached the western shelf of the Yucatan peninsula, closely following the bathymetry. The 1 dbar cluster has otherwise dispersed southward, northward, and eastward, so that after 100 days, surface drifters are scattered across the whole western GoM (west of 92°W). Dispersion of the float clusters at 300 and 1,500 dbar between 10 and 100 days seems more directional, as floats seem to mostly remain in the western end of the basin and to spread along its boundaries. After 100 days, the average distance from the launch location is 570, 390, and 285 km for the 1, 300, and 1,500 dbar floats, respectively.

Figures 6a–6c show that at all depths, floats preferentially drift along bathymetric contours. The ratio of along- and across-bathymetry velocity is consistently greater than 1 at all depths (average values of 1.3, 1.4, and 1.8 at 1, 300, and 1,500 dbar, respectively) but does not exhibit any particular coherent time trend, suggesting that topographic control of the float drifts at 1 and 1,500 dbar starts right after launching.

Time evolution of relative dispersion is shown in Figure 7a. At all depths, relative dispersion grows as a power function of time over a finite range of time: At the surface, it grows as $t^{2.1}$ between 2 and 35 days, while at 300 and 1,500 dbar, it grows as t^2 and $t^{1.8}$ in the time ranges (3–45) and (5–75) days, respectively. At

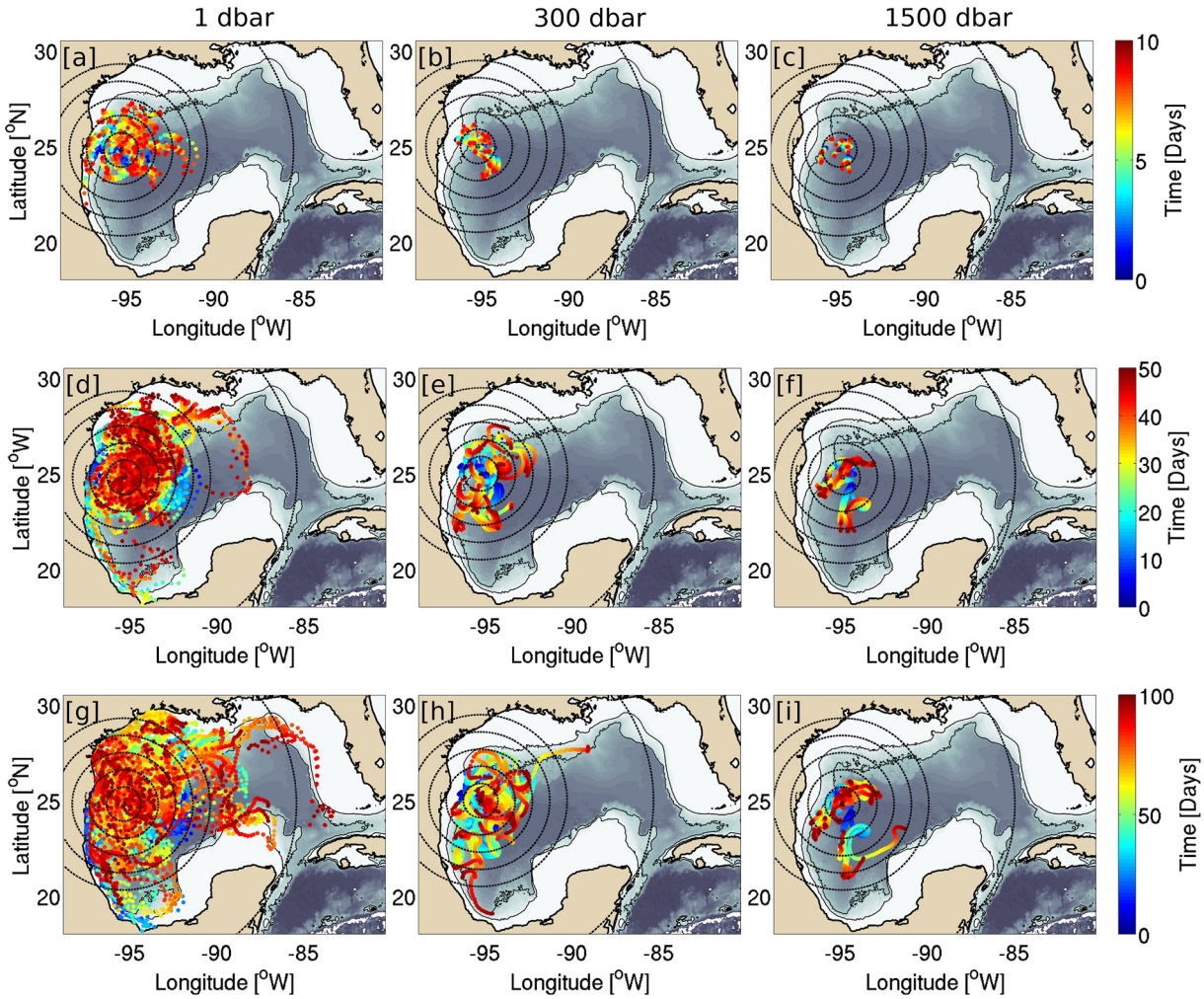

Figure 4. (a) Daily positions of surface drifters during the first 10 days. Time is color coded. Reference circles are plotted as dashed contours every 100 km. (b) Same as (a) for the 300 dbar RAFOS floats. (c) Same as (a) for the 1,500 dbar RAFOS floats. (d) Same as (a) for the first 50 days. (e) Same as (b) for the first 50 days. (f) Same as (c) for the first 50 days. (g) Same as (a) for the first 100 days. (h) Same as (b) for the first 100 days. (i) Same as (c) for the first 100 days.

longer time scales, the growth of relative dispersion becomes nearly linear with slopes of $t^{1.3}$, $t^{0.9}$, and $t^{1.4}$ at 1, 300, and 1,500 dbar, respectively. Time evolution of dispersion at short time scales is shown in Figure 7b. The exponential growth rate of dispersion was computed as $\gamma(t) = \frac{ln(D^2(t)) - ln(D^2(0))}{t}$ and is shown in Figure 7c: at all depths, the growth rates increase during the first 1–3 days, before reaching a maximum and decaying. Also evident in the time evolution of dispersion in Figure 7a is that the growth rate decreases with increasing depth. By nondimensionalizing time with the inverse maximum growth rate $\tilde{t} = t/\tau$, with $\tau = max(\gamma)^{-1}$, the exponential growth of dispersion at short time becomes discernible (Figure 7d). At all depths, the exponential regime is limited to a period of approximately 2τ, corresponding to dimensional times of ≈2, 3, and 5 days at 1, 300, and 1,500 dbar, respectively. For comparison, the 1 dbar pair dispersion was also computed using a downgraded temporal resolution that matches the RAFOS resolution of 8 h. The growth of low resolution dispersion is initially slower than that of the original resolution during the first 2 days (*e*-folding time of 1 day for the 8 h resolution and 0.6 days for the 1 h resolution). After day 2, the growth of dispersion is not sensitive to time resolution any more.

The impact of topography on pair separation was investigated using the along- and across-bathymetry components of pair separation velocities. The along- and across-bathymetry velocity ratios exhibit a slight anisotropy increasing with depth, with values of 1.1, 1.2, and 1.4 at 1, 300, and 1,500 dbar, respectively (Figures 6d–6f). As for absolute velocity ratios, no clear time dependence is observed. It seems important to

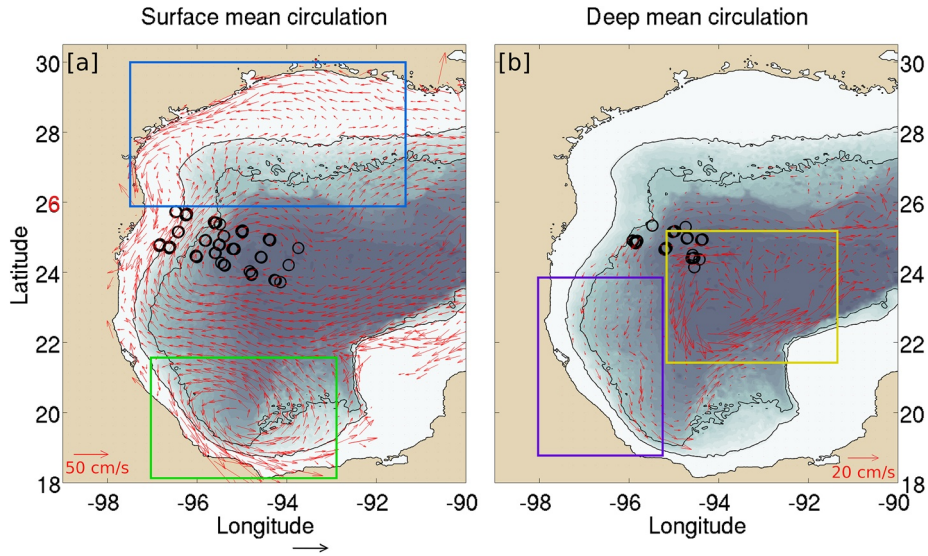

Figure 5. (a) Mean surface circulation from Lilly and Pérez-Brunius (2021)'s GulfFlow gridded product. The Campeche cyclonic gyre is indicated by the green box and the north-western boundary current by the blue box. (b) Mean deep (1,500–2,500 m) circulation from Pérez-Brunius et al. (2018). The south-western boundary current is indicated by the purple box and the Sigsbee abyssal gyre by the yellow box. The initial position of the surface drifters and RAFOS floats are shown as black circles.

note that these results, rather than being an homogeneous representation of the whole western basin might reflect the sum of subregional particular patterns. For instance, near-surface floats in the central-western basin should be much less sensitive to the topography and drift (or disperse) much more isotropically than floats drifting in the northern boundary current. The average along-/across-bathymetry velocity ratios were computed for the four subregions of interest described in Figure 5. Absolute and relative velocity ratios (respectively $\mathcal{R}_a$ and $\mathcal{R}_r$) at all depths are presented in Table 2. At 1 dbar, topographic control is evident as a significant anisotropy ($\mathcal{R}_a$ and $\mathcal{R}_r > 1$) in the northern and western boundary currents and in the Campeche gyre, while dispersion is nearly isoptropic in the Sigsbee abyssal plain area. Similar results are found at 300 dbar while the situation is much different at 1,500 dbar, where the Sigsbee abyssal plain's dispersion is

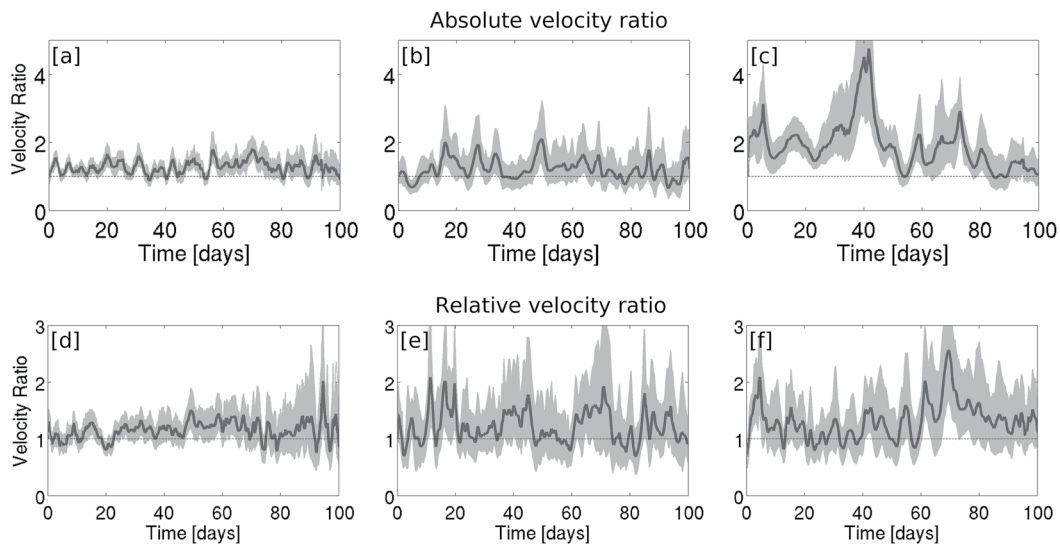

Figure 6. (a) Mean ratio of the along- and across-bathymetry components of absolute velocity against time at 1 dbar. (b) Same as (a) at 300 dbar. (c) Same as (a) at 1,500 dbar. (d) Mean ratio of the along- and across-bathymetry components of relative velocity against time at 1 dbar. (e) Same as (d) at 300 dbar. (f) Same as (d) at 1,500 dbar.

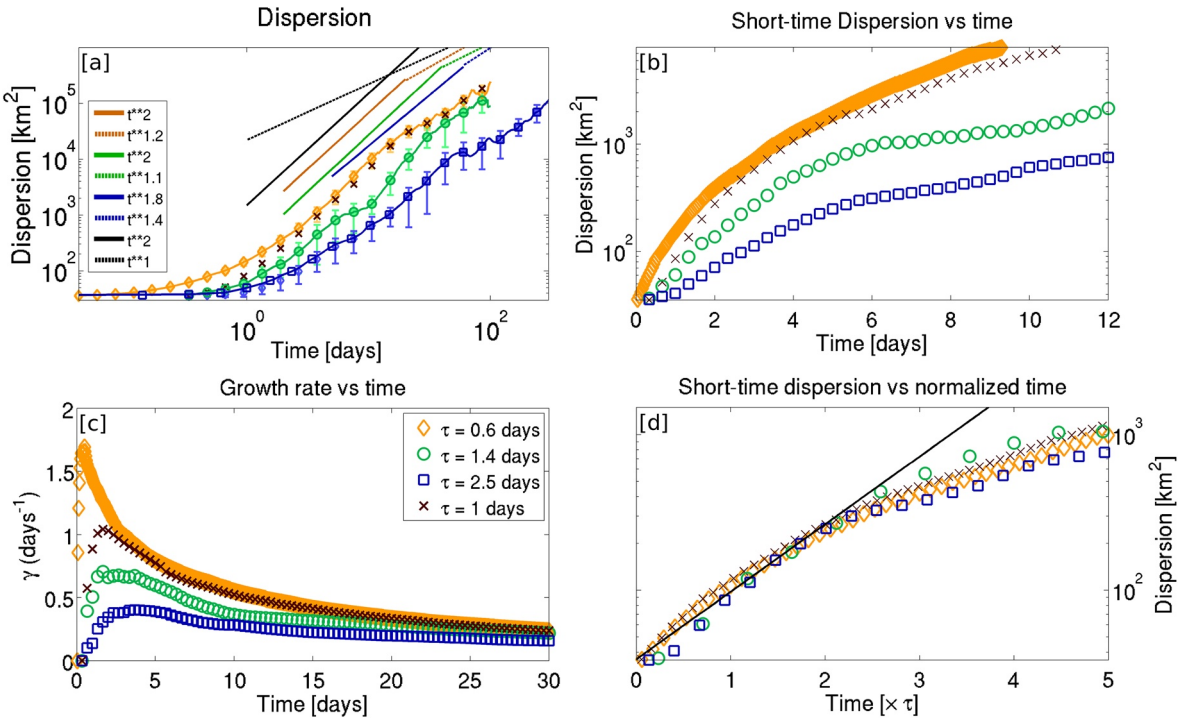

Figure 7. (a) Relative dispersion against time for the surface drifters (orange diamonds), 300 dbar (green circles), and 1,500 dbar RAFOS floats (blue squares). Linear fits at all depths are shown as continuous and dashed lines. The slopes are provided in the text box. (b) Short-time relative dispersion. (c) Growth rate γ against time. The e-folding time τ corresponding to the largest growth rate is indicated in the text box. (d) Same as (b) using a nondimensional time frame. Time is normalized by the inverse of the maximum growth rate at each depth ($\tilde{t} = 1/\tau$, where $\tau = max(\gamma)^{-1}$). The dashed gray line represents an exponential growth ($e^{\tilde{t}}$). Black crosses represent calculations from the 8 hourly resampling of the hourly surface drifter data.

consistent with strong anisotropy, likely driven by the Sigsbee gyre. At all depths and in all regions, topographic anisotropy is stronger for absolute velocity than relative velocity.

Time evolution of the pair separation kurtosis at 1, 300, and 1,500 dbar is shown in Figures 8a–8c, respectively. At all depths, the kurtosis follows the same pattern: after an initial period of growth, it approaches the Richardson's value (5.6) and then regularly decays to converge toward a value of 2 (indicative of the Rayleigh regime). The maximum kurtosis at 1, 300, and 1,500 dbar is of 7.4, 5.2, and 5.6, respectively. It is reached after 4 days at 1 and 300 dbar, and after 30 days at 1,500 dbar. Note that convergence toward the Rayleigh regime is significantly slower at 1,500 dbar than at the surface and subsurface. Figures 8d and 8e show the short-time evolution of the kurtosis. In panel e, time was nondimensionalized using the inverse maximum growth rate, computed as $\tilde{t}_k = 1/\tau_k$, with $\tau_k = max(\gamma_k)^{-1}$, and $\gamma_\iota = ln(Ku(t)/Ku(0))/t$. An initial exponential growth is evident at all depths in the nondimensional time frame. The exponential growth is limited to 1 τ_k, corresponding to dimensional times of 1.2, 1.1, and 2.2 days at 1, 300, and 1,500 dbar, respectively. As for dispersion in Figure 7, we computed the kurtosis using subsampled separation time series. As

Table 2
Ratio of the Along- and Across-Bathymetry Components of the Mean Absolute ($\mathcal{R}_a$) and Relative ($\mathcal{R}_r$) Velocity at 1, 300, and 1,500 dbar in Four Different Regions of the Western Gulf of Mexico

	1 dbar		300 dbar		1,500 dbar	
	$\mathcal{R}_a$	$\mathcal{R}_r$	$\mathcal{R}_a$	$\mathcal{R}_r$	$\mathcal{R}_a$	$\mathcal{R}_r$
Northern boundary	1.34 ± 0.01	1.0 ± 0.02	1.28 ± 0.09	0.9 ± 0.1	2.7 ± 1.1	N.A.
Western boundary	1.54 ± 0.03	1.3 ± 0.03	1.37 ± 0.07	1.23 ± 0.007	2.3 ± 0.07	1.62 ± 0.05
Campeche bay	1.95 ± 0.05	1.16 ± 0.05	1.74 ± 0.13	1.07 ± 0.08	1.99 ± 0.06	1.31 ± 0.07
Sigsbee abyssal plain	0.99 ± 0.01	1.15 ± 0.01	1.00 ± 0.01	1.09 ± 0.05	1.83 ± 0.03	1.21 ± 0.04

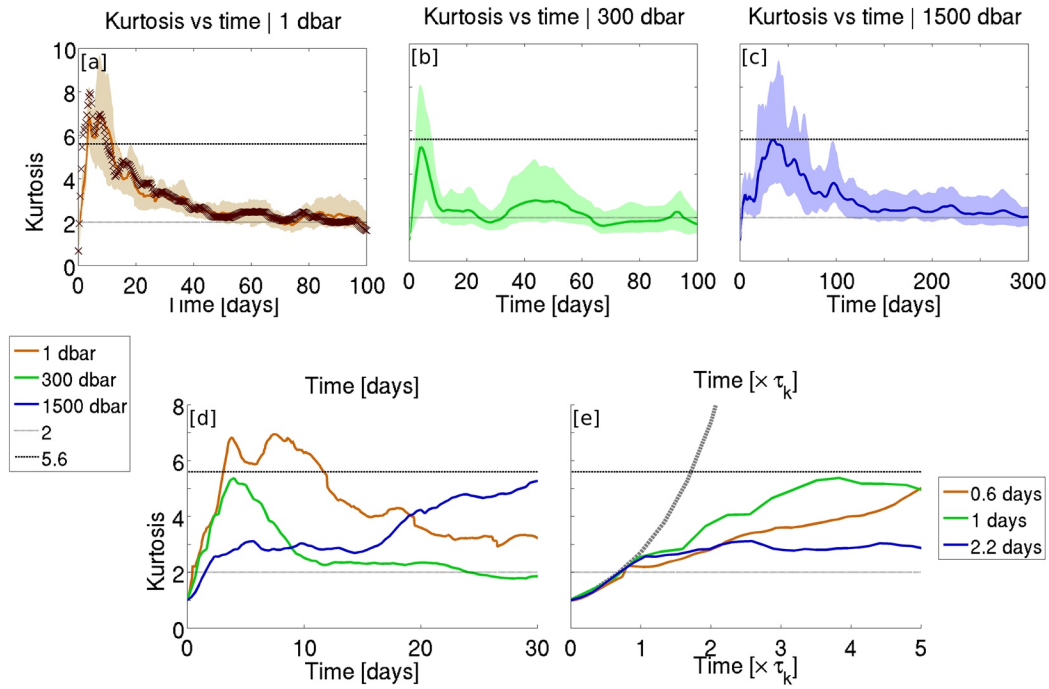

Figure 8. Pair separation kurtosis against time at (a) 1 dbar, (b) 300 dbar, and (c) 1,500 dbar. Black crosses represent calculations from the 8 hourly resampling of the hourly surface drifter data. A focus on short-time evolution is shown in panels (d) and (e). In panel (e), time was nondimensionalized by the inverse maximum growth rate ($\tilde{t}_k = 1/\tau_k$, with $\tau_k = max(\gamma_k)^{-1}$, and $\gamma_k = ln(Ku(t)/Ku(0))/t$). Exponential growth is represented by the dashed gray line.

evident in Figure 8a, the kurtosis is insensitive to the time resolution and can thus be used to compare the surface and deep floats.

Relative diffusivity at 1, 300 and 1,500 dbar is compared in Figure 9a. At all depths, the growth of relative diffusivity with increasing separation scale is close to the Richardson law $K \propto D^{4/3}$ ($D^{1.3}$, $D^{1.4}$, and $D^{1.6}$ at 1, 300, and 1,500 dbar, respectively) for scales of 10/20 km to 100 km and then saturates to approximately twice the single-particle diffusivity (≈18,000 [9,000–24,000], 5,000 [2,800–11,000], and 2,400 [1,700–3,300] $m^2\ s^{-1}$ at 1, 300, and 1,500 dbar, respectively). At shorter length scale ([6–20], [6–15], and [6–10] km at 1, 300, and

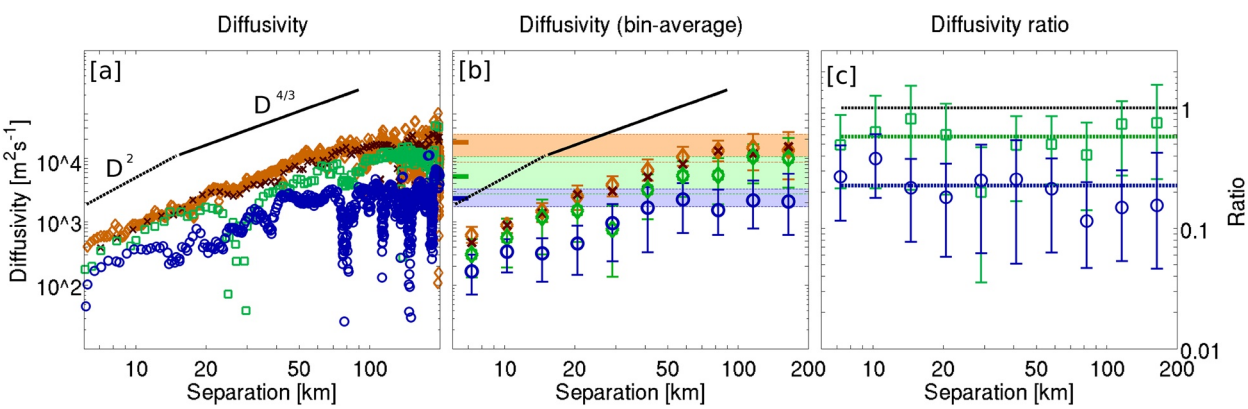

Figure 9. Relative diffusivity against separation. (a) Raw diffusivity. The orange diamonds represent the surface data, while the green squares and blue circles represent the 300 and 1,500 dbar data, respectively. The dotted and continuous black lines illustrate D^2 and $D^{2/3}$ growths, respectively. (b) Separation-averaged diffusivity: diffusivity was averaged over geometrically growing separation bins. The thick colored ticks on the left hand side represent the single-particle diffusivity at each depth. The 95% confidence interval for single-particle diffusivity is represented by the colored shaded areas. (c) Ratio of the diffusivity at depth and the surface diffusivity. The horizontal dashed lines represent the average value for each depth. Black crosses represent calculations from the 8 hourly resampling of the hourly surface drifter data.

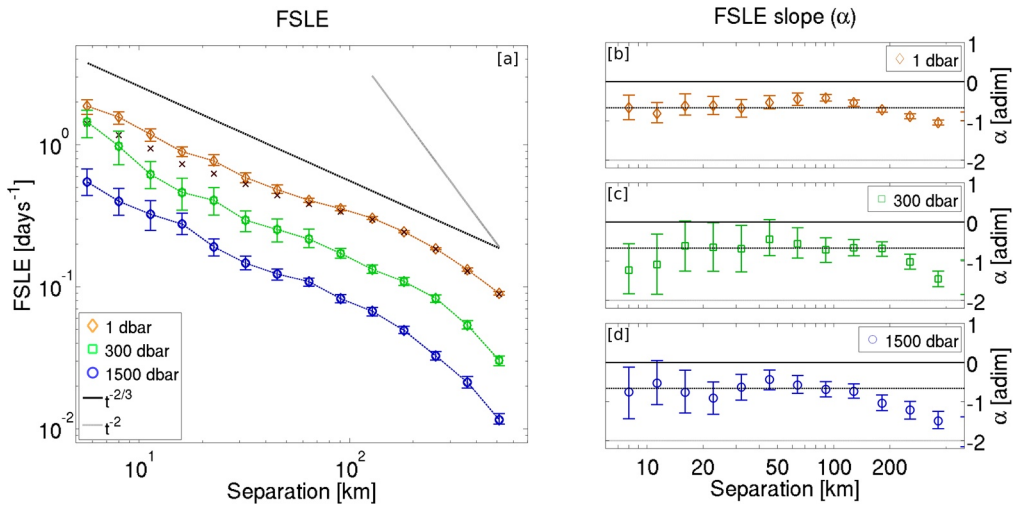

Figure 10. (a) Finite time Lyapunov exponent (FSLE) against separation scale at 1 dbar (orange diamonds), 300 dbar (green circles), and 1,500 dbar (blue squares). The dashed black line represent a $D^{-2/3}$ decay law, while the gray line represents a D^{-2} decay law. (b–d) Exponent (slope of the FSLE in the log–log diagram) for the (b) 1 dbar, (c) 300 dbar, and (d) 1,500 dbar data sets. Black crosses represent calculations from the 8 hourly resampling of the hourly surface drifter data.

1,500 dbar, respectively), the steeper slope is close to the D^2 growth expected in the exponential regime ($K \propto D^{1.8}$, $D^{2.2}$, and $D^{2.2}$ at 1, 300, and 1,500 dbar). Note however that the error bar is large, and although the fitted slopes coincide with theoretical expectations, a variety of slopes can fit through the 95% confidence interval (Figure 9b), so that the exponential regime at scales smaller than 10/20 km is only one possibility.

To assess the decrease of relative diffusivity with depth, we computed the ratio of the 300 and 1,500 dbar relative diffusivity to that at 1 dbar (Figure 9e). Relative diffusivity was first averaged over geometrically growing separation bins ranging from 5 to 300 km (the separation set used for FSLE computation). At all resolved scales, relative diffusivity decreases with depth. Although uncertainties are large, we found that relative diffusivity is respectively 1–5 times (average of 2) and 3–12 times (average of 5) smaller at 300 and 1,500 dbar than at the surface. No evident scale dependence of the diffusivity ratio could be found. Again, it is important to note that these values must be interpreted with care, given the large uncertainties.

The FSLEs at 1, 300, and 1,500 dbar are plotted against the separation scale in Figure 10a. The corresponding decay law ($\lambda \propto D^{\alpha}$) is shown in panels b, c, and d for the 1, 300, and 1,500 dbar data, respectively. At 1 dbar, FSLE follows a clear $D^{-2/3}$ decay law from the smallest resolved scales up to scales of about 200 km. The slope then steepens with increasing separation scales, possibly converging toward the Rayleigh regime slope (D^{-2}), although this value is never reached at the scales resolved in this study. At 300 and 1,500 dbar, error bars are larger and the decay law is not as clear: while the average slope is generally close to $D^{-2/3}$, consistent with Richardson law, the 95% confidence interval includes the possibility of a D^{-1} decay, indicative of a ballistic regime. At scales larger than 150–200 km, an increased decay of FSLE toward the standard diffusivity slope (D^{-2}) is also observed, consistent with a transition toward the Rayleigh regime.

To assess the dependence of our results to the initial pair separation, a sensitivity analysis was performed, varying initial separation from 1.5 to 48 km. Results from this analysis are presented in Figure 11. They are in total agreement with Balwada et al. (2021), who compared relative dispersion, kurtosis, and relative diffusivity for initial separations of 10, 30, and 50 km in the deep Antarctic Circumpolar Current. At all depths, the transition of relative dispersion from exponential to a power law is sensitive to initial separation (Figures 11a, 11d, and 11e): the smaller the initial separation, the sooner the transition into a power law. All cases however converge toward a t^1 law in the long time limit. Because of this convergence, and the different initial relative dispersions, the slopes in the intermediate time regime are sensitive to initial separation: the smaller the initial separation, the steepest the slope. Note that for very large initial separations (24–48 km), the slope at intermediate time scales is close to t^1, while for small initial separations (1.5 km), it becomes

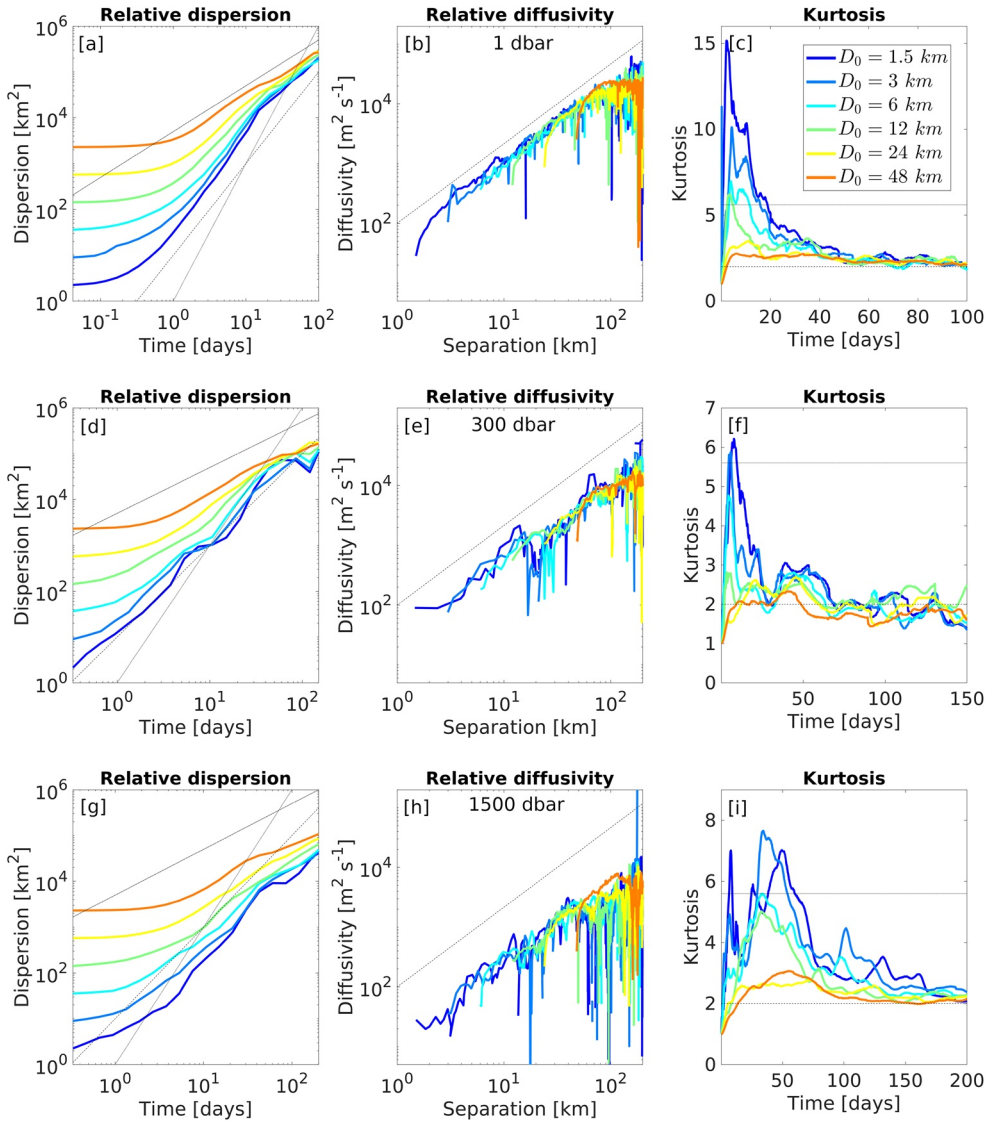

Figure 11. (a) The 1 dbar relative dispersion against time for six different initial pair separations (D_0 = 1.5, 3, 6, 12, 24, and 48 km.). (b) The 1 dbar relative diffusivity against pair separation for the six same initial separations. (c) The 1 dbar kurtosis against time for the six same initial separations. (d) Same as (a) at 300 dbar. (e) Same as (b) at 300 dbar. (f) Same as (c) at 300 dbar. (g) Same as (a) at 300 dbar. (h) Same as (b) at 300 dbar. (i) Same as (c) at 300 dbar. Line colors are described in the legend of panel (c). Gray dashed lines correspond to Richardson, ballistic and Rayleigh regimes for relative dispersion; Richardson regime for relative diffusivity; and exponential and Rayleigh regimes for Kurtosis.

steeper than t^2. Initial separation also has a strong impact on kurtosis (Figures 11c, 11f, and 11i): the smaller the initial separation, the larger and the sharper the kurtosis peak. For very large initial separations, kurtosis rapidly converges toward the diffusive regime ($Ku = 2$), without ever reaching near-Richardson values ($Ku = 5.6$), consistent with the t^1 slope of relative dispersion at intermediate time ranges. On the other hand, as expected for scale-dependent variables, relative diffusivity is not sensitive to the initial pair separation: all curves share the same slope and magnitude and are nearly superimposed.

4. Discussion and Conclusion

Values of the asymptotic saturation of surface relative diffusivity at scales larger than O(100 km; Taylor diffusivity, found in the Rayleigh regime) appear to belong to the high end of the World ocean's observed range. Zhurbas and Oh (2004)'s atlas of surface drifter-based absolute diffusivity shows that values larger

than O(10^4 m^2 s^{-1}), similar to our estimates of the surface GoM, are only reached in the equatorial currents, north of the subtropical gyres, and in the western boundary currents and their offshore extensions. Our estimates are however of the same order of magnitude as Koszalka et al. (2009)'s observations in the Nordic seas (O[2,000 km^2 day^{-1} ≈ 23,000 m^2 s^{-1}]). At a more regional scale, it is interesting to note that it closely matches Mariano et al. (2016)'s and Zavala Sansón et al. (2018)'s surface drifter-based values for the northern and south-western GoM, respectively (≈ 10^4 m^2 s^{-1}), suggesting that surface diffusivity in the GoM is not only high but also homogeneous across the basin.

It is important to recall that the drifters used in the DWDE had shallow drogues (1 m), while some of the aforementioned studies used deeper drogues (15 m in Zhurbas and Oh, 2004 and Koszalka et al., 2009; 50 m in Zavala Sansón et al., 2018]), so that direct comparison may seem, at first sight, difficult. Shallow-drogued drifters (0.5/1 m) measure the ocean's surface boundary layer (OSBL) motion, which is directly affected by wind and waves, while deeper-drogued drifters (15/50 m) primarily measure geostrophic turbulent dispersion. While wind-driven flows, such as Langmuir circulations, were shown to be a leading-order dispersion process at scales of O(100 m; Ohlmann et al., 2019), other recent modeling studies suggest that their impact, and that of OSBL processes in general, might be minor at the scales considered here. Using large eddy simulations, Liang et al. (2018) studied in details the dispersion properties of Langmuir circulations and waves, showing that at scales greater than 100 m, the latter was weaker than the dispersion by submesoscale flows (sharp fronts and high-Rossby number eddies). Herterich and Hasselmann (1982) estimated that Stokes drift-driven diffusivity saturates at scales of 100 and 1,000 m for wind speeds of 10 and 20 m s^{-1}, respectively. While the ability of models to accurately represent these processes may be questioned, the minor effect of OSBL processes on pair dispersion at larger scales was also demonstrated by Corrado et al. (2017) using observations. They showed, using large drifter numbers in the global ocean, that pairs of 15 m-drogued drifters and pairs of undrogued drifters exhibit very similar FSLE slopes at scales of 5–1,000 km. This suggests that turbulent dispersion dominates over OSBL effects, even at shallow depths. Note also that recent Lagrangian observations in the GoM by Balwada, LaCasce, et al. (2016) demonstrated that pair dispersion was influenced by divergent motion (likely attributable to OSBL) only at scales smaller than 5 km. Dispersion and diffusivity estimates from shallow-drogued drifters, as used in the present study, as well as previous studies in the northern GoM (Mariano et al., 2016; Poje et al., 2014), are thus expected to be directly comparable with estimates from 15 m-drogued drifters at the scales resolved here ([5–300] km), and particularly at the large-separation scales of the Rayleigh regime discussed above.

Since little observation-based estimates of diffusivity are available at 300 and 1,500 dbar, direct comparison with other regions of the ocean is limited. Using isopycnal RAFOS floats, LaCasce and Bower (2000) and Zhang et al. (2001) provided estimates of large-scale-saturated relative diffusivity at five different sites of the North Atlantic and in different depth ranges. More recently, LaCasce et al. (2014), Balwada, Speer, et al. (2016), and Balwada et al. (2021) estimated diffusivity from RAFOS floats in the Southern Ocean at depths ranging between 500 and 2,000 m. Here, we found large-scale saturation values for relative diffusivity (Taylor diffusivity) of ≈9,000 and ≈4,000 m^2 s^{-1} at 300 and 1,500 dbar, respectively. These are small in comparison to LaCasce and Bower (2000) and Zhang et al. (2001)'s values in the [100–900 m] range in the North Atlantic Current off Newfoundland, and at 700 m offshore of the Gulf Stream's eastern flank (≈30,000 and ≈40,000 m^2 s^{-1}, respectively) but are surprisingly larger than Southern Ocean values of ≈1,000 m^2 s^{-1} (Balwada, Speer, et al., 2016; Balwada et al., 2021; LaCasce et al., 2014). Our estimate of the 1,500 dbar maximum relative diffusivity is, however, of the same order of magnitude as at 1,000 m in the Mediterranean Outflow and at 1,300 m in the Gulf Stream region (≈ 6,000 m^2 s^{-1}; LaCasce & Bower, 2000).

Since deep dispersion is essentially isopycnal, it seems relevant to discuss the validity of the lateral diffusivity inferred from isobaric floats to represent isopycnal diffusivity. The latter evidently depends on the slope of the isopycnals in the western GoM. In the presence of sharp fronts, water parcels move freely along the isopycnals and are displaced upward or downward while isobaric floats remain at the same pressure level. This might result in artificial divergence or convergence of floats that are constrained to a given depth. This issue is in all points similar to the dispersion of floating objects in the presence of intense horizontal convergence. While continuity is ensured by downwelling of the water parcels, buoyancy prevents the floats and drifters from sinking, resulting in accumulation at fronts and bias of the dispersion statistics (Miron et al., 2020). While this well-known issue is difficult to solve or even quantify, it has been underlying the

results of all surface dispersion experiments over the past decades. However, its effects on deep floats should be more modest than on surface drifters since the lower Rossby numbers usually found at depth suggest that divergence should be weaker than in sharp surface fronts. While, to the best of our knowledge, no direct synoptic Eulerian observation of the deep density structure is available for the western GoM, at shallower depths, Meunier et al. (2018) sampled the density structure of a Loop Current Ring (LCR) drifting in the central-western GoM and showed that the isopycnal slopes on the edge of the eddy were of about 2/1,000 between 200 and 400 m and of 1.5/1,000 between 800 and 1,000 m. LCRs were shown to be the most energetic features of the GoM, and the isopycnal sloping at their boundaries, therefore, belongs to the very high end of the GoM's isopycnal slopes range. The projection of lateral diffusivity on such small isopycnal slopes would yield insignificant differences between lateral and isopycnal diffusivity, so that we should expect our estimates of lateral diffusivity to be a solid proxy for isopycnal diffusivity.

Most importantly, our results highlight the depth dependence of relative dispersion on scales of [6–150 km] from floats that were released simultaneously at all depths. The DWDE thus provides one of the first estimates of the variation of relative diffusivity with depth at the same time and place. We found that, averaging over all separation scales, relative diffusivity at 300 dbar is about 2 times smaller than at the surface (range 1–5), while it is about 5 times smaller at 1,500 dbar (range 2–12). The seemingly scale independence of the ratio of subsurface to surface diffusivity may result from the similar growth law of relative diffusivity with separation scale ($\propto D^{4/3}$) at all depths in the (10–100 km) range, but this result is subject to large uncertainty, and would require larger data sets to be confirmed.

This study also partially revealed the turbulence regimes occurring at all three depths, although some ambiguity remains. As repeatedly reported in the literature, Lagrangian diagnoses from real ocean observations offer an incomplete description of the turbulent regimes when looked at separately and sometimes yield contradictory information when compared to one another. This is particularly true when comparing time-dependent variables, such as relative dispersion or kurtosis, with separation scale-dependent variables such as relative diffusivity or FSLE (Beron-Vera & LaCasce, 2016; Koszalka et al., 2009). More specifically, the GoM violates two important assumptions of the 2D turbulence theory: the domain is bounded and is not large compared to the scale of some energetic eddies (a typical LCR can reach 300 km in diameter Meunier et al., 2020, while the meridional extension of the basin is of about 900 km), and the turbulence is not stationary, as episodic LCR shedding likely modifies the western basin's dynamical properties in the surface layer as the eddies reach the continental shelf and split into numerous smaller eddies (Biggs et al., 1996; Lipphardt et al., 2008), and in the deep layer as the dipole traveling below the LCR reaches the continental slope (Tenreiro et al., 2018).

In particular, while the relationship between FSLE and separation scale at 1 dbar seems straightforward and clearly indicative of a Richardson regime ($\propto D^{-2/3}$) at scales of [6–100] km, in good agreement with the growth of relative diffusivity as $\propto D^{4/3}$, dispersion was found to have a quadratic growth, consistent with ballistic (or shear) dispersion (LaCasce & Ohlmann, 2003). However, in the case of ballistic dispersion, FSLE should decay as $\propto D^{-1}$, and relative diffusivity grows as $\propto D^{1}$. At 300 and 1,500 dbar, although the average FSLE decay is close to $\propto D^{-2/3}$, indicative of a Richardson regime, the $\propto D^{-1}$ decay law associated with ballistic dispersion is included in the 95% confidence interval. The latter regime is also suggested by the growth of dispersion with time $D^2 \propto t^2$. It seems difficult to definitively discriminate between one regime or the other or the possibility of both occurring simultaneously. It should be pointed out that the fact that the time-dependent metrics suggest a different regime than space-dependent metrics might be an artifact of the decrease of pairs in time (Figure 3) deteriorating or biasing the statistics at long times. Koszalka et al. (2009) and LaCasce (2008) noted that the joint use of both types of diagnostics was often necessary and sometimes contradictory. Ballistic regimes are a common feature of closed or semienclosed basins and were identified in the Mediterranean Sea (Iudicone et al., 2002), the Adriatic Sea (Haza et al., 2008), the North Sea (Meyerjürgens et al., 2020), as well as in previous studies of the GoM (LaCasce & Ohlmann, 2003). Haza et al. (2008) explained the presence of a ballistic regime in the Adriatic Sea as the consequence of the presence of persistent boundary currents which are associated with a sheared mean flow. By eliminating boundary currents from their modeled velocity field, they showed that the ballistic regime switched to Richardson's regime. We believe that these arguments would make sense in the case of the western GoM: at all depths, the mean flow is characterized by boundary currents (along the north-western and south-western shelves at the surface and along the western boundary and around the Sigsbee abyssal escarpment at depth;

Lilly & Pérez-Brunius, 2021; Pérez-Brunius et al., 2018). These topographic features were shown to have an evident influence on the drifter's trajectory, with significantly larger mean along-bathymetry velocity component. Despite large uncertainties, larger along-bathymetry pair separation velocity was also observed, supporting the idea of an influence of boundary currents on relative dispersion.

At short time and space scales, the relationship between relative dispersion and time, kurtosis and time, and between relative diffusivity and separation only shows discussable and ambiguous evidence of a possible exponential regime. While the initial growths of dispersion and kurtosis both seem close to exponential, the growth rates are not constant as expected from a true exponential regime, and the maximum kurtosis growth rate is approximately twice that of dispersion, while theory predicts that they should be the same (Beron-Vera & LaCasce, 2016). The increased slope of diffusivity in the [6–15] km range would also weakly suggest a possible exponential regime, but the error bars are far too large to be conclusive. The closed-basin constraint was shown to be an important limiting factor when trying to infer turbulent regimes from relative diffusivity. Artale et al. (1997) showed that the use of FSLEs was more accurate to discriminate between possible regimes, and this method was successfully applied to infer the regime shift between nonlocal (exponential) and local (Richardson) in a number of studies (LaCasce, 2008; LaCasce & Ohlmann, 2003; Lacorata et al., 1999). Here, at all depths, FSLEs exhibit an approximate $D^{-2/3}$ law over the entire resolved scale range, while the existence of an exponential regime should materialize as constant FSLEs at scales smaller than most energetic eddies size.

This suggests that there might not be any dominant eddy-size under which the energy would collapse, so that the energy spectrum might be flatter than the expected k^{-3}. Such a flat spectrum at scales that are way below the first Rossby radius could be indicative of intense submesoscale activity, similar to the results of Poje et al. (2014) in the surface northern GoM, although large uncertainties do not allow to definitively conclude on this point. It should also be pointed out that such steep FSLEs at small scale could also result from intense near-inertial wave activity (Balwada et al., 2021).

Because the boundary of enclosed basins can limit the dispersion of particles before the full decorrelation of particle velocities naturally yields a regime shift toward standard diffusion (Rayleigh regime), the long time and large-scale limit of the dispersion properties in the GoM deserves further discussion. A transition toward a linear growth of relative dispersion was evident at all depths, suggesting a regime shift toward Rayleigh regime. The saturation of relative diffusivity at scales of (100–150 km) also supports this possibility. However, recent work from Flores Ramírez and Zavala Sansón (2019) showed that bounded domains could result in a saturation regime, where the growth of relative dispersion is limited to an upper bound of R^2 for circular basins with radius R, or $L^2/4$ for squared basins of side L. While such a saturation of dispersion should be accompanied by a collapse of relative diffusivity, which is not observed here, the maximum observed surface dispersion after 150 days nearly reaches the saturation dispersion, considering the western GoM as a circular basin of radius $R = 450$ km. In the case of topography-saturated dispersion, pair separation kurtosis should decay and converge toward a value of 1.67. In the present work, the confidence interval is too large to be conclusive, and we cannot exclude possible saturating effects of the basin's geometry.

The peculiarities of the GoM's geometry and intermittent dynamics may not allow a direct generalization of our results to the variation of dispersion with depth in the ocean in general. New experiments, in a larger and open basin, would be useful. Such experiments should include an increased number of sampled depths, from the seafloor to the surface to more accurately assess the vertical distribution of diffusivity in oceanic turbulence.

5. Summary

As is often the case with observation-based dispersion studies, in particular when inertial ranges are finite, a clear identification of the dispersion regimes is difficult and relies on the use of several metrics. The scaling laws found at each depth for each variable, as well as their ranges of validity, are summarized in Table 3, along with the possible regimes and the associated theoretical expectations. The main conclusions of this study, inferred from the results recalled in Table 3, can be summarized as follows:

1. At small scales, the existence of nonlocal dispersion remains unclear, with ambiguous results. While time-based metrics suggest the existence of an exponential regime at all depths, separation-based metrics indicate a Richardson regime down to the smallest resolved scales.

Table 3
Summary of the Possible Regimes Observed in the DWDE Data Set as Inferred From the Different Diagnostic Variables

	Regime	Lundgren (exponential)	Richardson	Ballistic	Rayleigh
$D^2(t)$	Theory	$D_0^2 e^{\gamma t}$	$\propto t^3$	$\propto t^2$	$\propto t^1$
	1 dbar	[0-2] days	not observed	[2-35] days ($t^{2.1}$)	>35 days ($t^{1.3}$)
	300 dbar	[0-3] days	not observed	[3-45] days (t^2)	>45 days ($t^{0.9}$)
	1500 dbar	[0-5] days	not observed	[5-75] days ($t^{1.8}$)	>75 days ($t^{1.4}$)
$Ku(t)$	Theory	$e^{\gamma t}$	5.6	–	2
	1 dbar	[0-1] days	[1-50] days (≈7.4)	[1-50] days (≈7.4)	>50 days (≈2)
	300 dbar	[0-1] days	[1-30] days (≈5.2)	[1-30] days (≈5.2)	>30 days (≈2)
	1500 dbar	[0-2] days	[2-120] days (≈5.6)	[2-120] days (≈5.6)	>120 days (≈2)
$K(D)$	Theory	$\propto D^2$	$\propto D^{4/3}$	$\propto D^2$	cst.
	1 dbar	[6-20] km ($D^{1.8}$)	[20-100] km ($D^{1.3}$)	within uncertainty range	>100 km (18.000 $m^2\ s^{-1}$)
	300 dbar	[6-15] km ($D^{2.2}$)	[15-100] km ($D^{1.4}$)	within uncertainty range	>100 km (5.000 $m^2\ s^{-1}$)
	1500 dbar	[6-10] km ($D^{2.2}$)	[10-100] km ($D^{1.6}$)	within uncertainty range	>100 km (2.400 $m^2\ s^{-1}$)
$\lambda(D)$	Theory	cst.	$D^{-2/3}$	D^{-1}	D^{-2}
	1 dbar	not observed	[6-200] km ($\approx D^{0.6}$)	within uncertainty range	>150 km ($\approx D^{-1}$)
	300 dbar	not observed	[6-200] km ($\approx D^{0.7}$)	within uncertainty range	>150 km ($\approx D^{-1.5}$)
	1500 dbar	not observed	[6-150] km ($\approx D^{0.7}$)	within uncertainty range	>150 km ($\approx D^{-1.6}$)

Note. The time and spatial scale ranges are indicated and colored. Green indicates that the mean values of a given variable is consistent with a given regime, orange indicates that the uncertainty range of a given variable includes the regime, and red indicates that the given regime is outside of the uncertainty range for a given variable. The scaling laws are also indicated in black.

2. A similar ambiguity was found at intermediate scales: while time-based metrics are consistent with ballistic dispersion at all depths, separation-based metrics are in favor of a Richardson regime. Large uncertainties however do not allow to definitely rule out the possibility of a ballistic regime from the separation-based metrics.
3. Topographic anisotropy of dispersion, particularly evident near the basin's boundaries, suggests that boundary currents could play an important role in providing the horizontal shear, necessary for ballistic dispersion to occur.
4. At the surface, absolute (Taylor) diffusivity in the western GoM is elevated, with values among the largest observed in the World ocean.
5. At 300 and 1,500 dbar, on average, relative diffusivity is respectively 2 times smaller (range 1–5) and 5 times smaller (range 2–12), than at the surface.
6. No scale dependence of these ratios is evident in the present data set.

Data Availability Statement

Drifter and RAFOS float data available for nonprofit academic use at https://zenodo.org/record/3979964 and https://doi.org/10.5281/zenodo.4118564.

Acknowledgments
We appreciate early discussions with Luis Zavala Sanson, Joe LaCasce, and Javier Berón Vera about dispersion theory and Josefina Olascoaga on experimental setup. This research has been funded by the Mexican National Council for Science and Technology - Mexican Ministry of Energy - Hydrocarbon Fund, project 201441. This is a contribution of the Gulf of Mexico Research Consortium (CIGoM). We acknowledge PEMEX's specific request to the Hydrocarbon Fund to address the environmental effects of oil spills in the Gulf of Mexico.

References

Amante, C., & Eakins, B. W. (2009). *Etopo1 arc-minute global relief model: Procedures, data sources and analysis*.
Artale, V., Boffetta, G., Celani, A., Cencini, M., & Vulpiani, A. (1997). Dispersion of passive tracers in closed basins: Beyond the diffusion coefficient. *Physics of Fluids*, *9*(11), 3162–3171. https://doi.org/10.1063/1.869433
Aurell, E., Boffetta, G., Crisanti, A., Paladin, G., & Vulpiani, A. (1996). Growth of noninfinitesimal perturbations in turbulence. *Physical Review Letters*, *77*(7), 1262–1265. https://doi.org/10.1103/PhysRevLett.77.1262
Babiano, A., Basdevant, C., Le Roy, P., & Sadourny, R. (1990). Relative dispersion in two-dimensional turbulence. *Journal of Fluid Mechanics*, *214*, 535–557. https://doi.org/10.1017/S0022112090000258
Balwada, D., LaCasce, J. H., & Speer, K. G. (2016). Scale-dependent distribution of kinetic energy from surface drifters in the Gulf of Mexico. *Geophysical Research Letters*, *43*, 10856–10863. https://doi.org/10.1002/2016GL069405
Balwada, D., LaCasce, J. H., Speer, K. G., & Ferrari, R. (2021). Relative dispersion in the Antarctic Circumpolar Current. *Journal of Physical Oceanography*, *51*(2), 553–574. https://doi.org/10.1175/JPO-D-19-0243.1
Balwada, D., Speer, K. G., LaCasce, J. H., Owens, W. B., Marshall, J., & Ferrari, R. (2016). Circulation and stirring in the southeast Pacific Ocean and the Scotia Sea sectors of the Antarctic Circumpolar Current. *Journal of Physical Oceanography*, *46*(7), 2005–2027. https://doi.org/10.1175/JPO-D-15-0207.1
Batchelor, G. K. (1952). Diffusion in a field of homogeneous turbulence. *Proceedings of the Cambridge Philosophical Society*, *48*(2), 345–362. https://doi.org/10.1017/S0305004100027687
Bennett, A. F. (1987). A Lagrangian analysis of turbulent diffusion. *Reviews of Geophysics*, *25*, 799. https://doi.org/10.1029/RG025i004p00799
Bennett, A. F., & Denman, K. L. (1985). Phytoplankton patchiness: Inferences from particle statistics. *Journal of Marine Research*, *43*(2), 307–335. https://doi.org/10.1357/002224085788438711
Beron-Vera, F. J., & LaCasce, J. H. (2016). Statistics of simulated and observed pair separations in the Gulf of Mexico. *Journal of Physical Oceanography*, *46*(7), 2183–2199. https://doi.org/10.1175/JPO-D-15-0127.1
Biggs, D. C., Fargion, G. S., Hamilton, P., & Leben, R. R. (1996). Cleavage of a Gulf of Mexico Loop Current eddy by a deep water cyclone. *Journal of Geophysical Research*, *101*, 20629–20641. https://doi.org/10.1029/96JC01078
Charney, J. G. (1971). Geostrophic turbulence. *Journal of the Atmospheric Sciences*, *28*(6), 1087–1095. https://doi.org/10.1175/1520-0469(1971)028<1087:GT>2.0.CO;2
Colin de Verdiere, A. (1983). Lagrangian eddy statistics from surface drifters in the eastern North Atlantic. *Journal of Marine Research*, *41*(3), 375–398. https://doi.org/10.1357/002224083788519713
Corrado, R., Lacorata, G., Palatella, L., Santoleri, R., & Zambianchi, E. (2017). General characteristics of relative dispersion in the ocean. *Scientific Reports*, *7*, 46291. https://doi.org/10.1038/srep46291
Davis, R. E. (1991). Lagrangian ocean studies. *Annual Review of Fluid Mechanics*, *23*, 43–64. https://doi.org/10.1146/annurev.fl.23.010191.000355
Drazen, J. C., Smith, C. R., Gjerde, K. M., Haddock, S. H. D., Carter, G. S., Choy, C. A., et al. (2020). Opinion: Midwater ecosystems must be considered when evaluating environmental risks of deep-sea mining. *Proceedings of the National Academy of Sciences of the United States of America*, *117*(30), 17455–17460. https://doi.org/10.1073/pnas.2011914117
Flores Ramírez, L. M., & Zavala Sansón, L. (2019). Two-dimensional turbulence dispersion in a closed domain: Influence of confinement and geometry. *AIP Advances*, *9*(3), 035302. https://doi.org/10.1063/1.5081848
Hamilton, P., Leben, R., Bower, A., Furey, H., & Pérez-Brunius, P. (2018). Hydrography of the Gulf of Mexico using autonomous floats. *Journal of Physical Oceanography*, *48*(4), 773–794. https://doi.org/10.1175/JPO-D-17-0205.1
Haza, A. C., Poje, A. C., Özgökmen, T. M., & Martin, P. (2008). Relative dispersion from a high-resolution coastal model of the Adriatic Sea. *Ocean Modelling*, *22*(1), 48–65. https://doi.org/10.1016/j.ocemod.2008.01.006
Herterich, K., & Hasselmann, K. (1982). The horizontal diffusion of tracers by surface waves. *Journal of Physical Oceanography*, *12*(7), pp. 704–711. https://doi.org/10.1175/1520-0485(1982)012<0704:THDOTB>2.0.CO;2
Iudicone, D., Lacorata, G., Rupolo, V., Santoleri, R., & Vulpiani, A. (2002). Sensitivity of numerical tracer trajectories to uncertainties in OGCM velocity fields. *Ocean Modelling*, *4*(3), 313–325. https://doi.org/10.1016/S1463-5003(02)00006-9
Koszalka, I., LaCasce, J. H., & Orvik, K. A. (2009). Relative dispersion in the Nordic seas. *Journal of Marine Research*, *67*(4), 411–433. https://doi.org/10.1357/002224009790741102
Kraichnan, R. H. (1967). Inertial ranges in two-dimensional turbulence. *Physics of Fluids*, *10*(7), 1417–1423. https://doi.org/10.1063/1.1762301
Kujawinski, E. B., Kido Soule, M. C., Valentine, D. L., Boysen, A. K., Longnecker, K., & Redmond, M. C. (2011). Fate of dispersants associated with the Deepwater Horizon oil spill. *Environmental Science and Technology*, *45*(4), 1298–1306. https://doi.org/10.1021/es103838p
LaCasce, J. H. (2008). Statistics from Lagrangian observations. *Progress in Oceanography*, *77*(1), 1–29. https://doi.org/10.1016/j.pocean.2008.02.002
LaCasce, J. H., & Bower, A. (2000). Relative dispersion in the subsurface North Atlantic. *Journal of Marine Research*, *58*(6), 863–894. https://doi.org/10.1357/002224000763485737
LaCasce, J. H., Ferrari, R., Marshall, J., Tulloch, R., Balwada, D., & Speer, K. (2014). Float-derived isopycnal diffusivities in the DIMES experiment. *Journal of Physical Oceanography*, *44*(2), 764–780. https://doi.org/10.1175/JPO-D-13-0175.1
LaCasce, J. H., & Ohlmann, C. (2003). Relative dispersion at the surface of the Gulf of Mexico. *Journal of Marine Research*, *61*(3), 285–312. https://doi.org/10.1357/002224003322201205
LaCasce, J. H., & Speer, K. G. (1999). Lagrangian statistics in unforced barotropic flows. *Journal of Marine Research*, *57*(2), 245–274. https://doi.org/10.1357/002224099321618218
Lacorata, G., Aurell, E., & Vulpiani, A. (1999). *Drifters dispersion in the Adriatic Sea: Lagrangian data and chaotic model*. arXiv e-prints, chao-dyn/9902014.

Liang, J.-H., Wan, X., Rose, K. A., Sullivan, P. P., & McWilliams, J. C. (2018). Horizontal dispersion of buoyant materials in the ocean surface boundary layer. *Journal of Physical Oceanography*, *48*(9), 2103–2125. https://doi.org/10.1175/JPO-D-18-0020.1

Lilly, J., & Pérez-Brunius, P. (2021). A gridded surface current product for the Gulf of Mexico from consolidated drifter measurements. *Earth System Science Data Discussions*, *13*, 645–669.

Lin, J.-T. (1972). Relative dispersion in the enstrophy-cascading inertial range of homogeneous two-dimensional turbulence. *Journal of the Atmospheric Sciences*, *29*(2), 394–396. https://doi.org/10.1175/1520-0469(1972)029<0394:RDITEC>2.0.CO;2

Lipphardt, B., Poje, A., Kirwan, A., Kantha, L., & Zweng, M. (2008). Death of three loop current rings. *Journal of Marine Research*, *66*(1), 25–60. https://doi.org/10.1357/002224008784815748

Lundgren, T. S. (1981). Turbulent pair dispersion and scalar diffusion. *Journal of Fluid Mechanics*, *111*, 27–57. https://doi.org/10.1017/S0022112081002280

Mariani, P., MacKenzie, B., Visser, A., & Botte, V. (2007). Individual-based simulations of larval fish feeding in turbulent environments. *Marine Ecology Progress Series*, *347*, 155–169. https://doi.org/10.3354/meps07092

Mariano, A. J., Ryan, E. H., Huntley, H. S., Laurindo, L. C., Coelho, E., Griffa, A., et al. (2016). Statistical properties of the surface velocity field in the northern Gulf of Mexico sampled by GLAD drifters. *Journal of Geophysical Research: Oceans*, *121*, 5193–5216. https://doi.org/10.1002/2015JC011569

McNutt, M. K., Camilli, R., Crone, T. J., Guthrie, G. D., Hsieh, P. A., Ryerson, T. B., et al. (2012). Review of flow rate estimates of the Deepwater Horizon oil spill. *Proceedings of the National Academy of Sciences of the United States of America*, *109*(50), 20260–20267. https://doi.org/10.1073/pnas.1112139108

McWilliams, J. C. (1989). Statistical properties of decaying geostrophic turbulence. *Journal of Fluid Mechanics*, *198*, 199–230. https://doi.org/10.1017/S0022112089000108

Meunier, T., Sheinbaum, J., Pallàs-Sanz, E., Tenreiro, M., Ochoa, J., Ruiz-Angulo, A., et al. (2020). Heat content anomaly and decay of warm-core rings: The case of the Gulf of Mexico. *Geophysical Research Letters*, *47*, e2019GL085600. https://doi.org/10.1029/2019GL085600

Meunier, T., Tenreiro, M., Pallás-Sanz, E., Ochoa, J. L., Ruíz-Angulo, A., Damien, P., & Carton, X. (2018). Observations of intra-thermocline eddies embedded in an anticyclonic vortex ring. Manuscript submitted for publication.

Meyerjürgens, J., Ricker, M., Schakau, V., Badewien, T. H., & Stanev, E. V. (2020). Relative dispersion of surface drifters in the North Sea: The effect of tides on mesoscale diffusivity. *Journal of Geophysical Research: Oceans*, *125*, e2019JC015925. https://doi.org/10.1029/2019JC015925

Miron, P., Olascoaga, M. J., Beron-Vera, F. J., Putman, N. F., Triñanes, J., Lumpkin, R., & Goni, G. J. (2020). Clustering of marine-debris- and *Sargassum*-like drifters explained by inertial particle dynamics. *Geophysical Research Letters*, *47*, e2020GL089874. https://doi.org/10.1029/2020GL089874

Morel, P., & Larceveque, M. (1974). Relative dispersion of constant-level balloons in the 200-mb general circulation. *Journal of the Atmospheric Sciences*, *31*(8), 2189–2196. https://doi.org/10.1175/1520-0469(1974)031<2189:RDOCBI>2.0.CO;2

North, E. W., Adams, E. E., Schlag, Z., Sherwood, C. R., He, R., Hyun, K. H., & Socolofsky, S. A. (2011). Simulating oil droplet dispersal from the Deepwater Horizon spill with a Lagrangian approach. *Washington DC American Geophysical Union Geophysical Monograph Series*, *195*, 217–226. https://doi.org/10.1029/2011GM001102

Ohlmann, J. C., Romero, L., Pallàs-Sanz, E., & Perez-Brunius, P. (2019). Anisotropy in coastal ocean relative dispersion observations. *Geophysical Research Letters*, *46*, 879–888. https://doi.org/10.1029/2018GL081186

Ollitrault, M., Gabillet, C., & de Verdière, A. C. (2005). Open ocean regimes of relative dispersion. *Journal of Fluid Mechanics*, *533*, 381–407. https://doi.org/10.1017/s0022112005004556

Pérez-Brunius, P., Furey, H., Bower, A., Hamilton, P., Candela, J., García-Carrillo, P., & Leben, R. (2018). Dominant circulation patterns of the deep Gulf of Mexico. *Journal of Physical Oceanography*, *48*(3), 511–529. https://doi.org/10.1175/JPO-D-17-0140.1

Poje, A. C., Özgökmen, T. M., Bogucki, D. J., & Kirwan, A. D. (2017). Evidence of a forward energy cascade and Kolmogorov self-similarity in submesoscale ocean surface drifter observations. *Physics of Fluids*, *29*(2), 020701. https://doi.org/10.1063/1.4974331

Poje, A. C., Özgökmen, T. M., Lipphardt, J., Bruce, L., Haus, B. K., Ryan, E. H., et al. (2014). Submesoscale dispersion in the vicinity of the Deepwater Horizon spill. *Proceedings of the National Academy of Sciences of the United States of America*, *111*(35), 12693–12698. https://doi.org/10.1073/pnas.1402452111

Reddy, C. M., Arey, J. S., Seewald, J. S., Sylva, S. P., Lemkau, K. L., Nelson, R. K., et al. (2012). Composition and fate of gas and oil released to the water column during the Deepwater Horizon oil spill. *Proceedings of the National Academy of Sciences of the United States of America*, *109*(50), 20229–20234. https://doi.org/10.1073/pnas.1101242108

Rhines, P. B. (1979). Geostrophic turbulence. *Annual Review of Fluid Mechanics*, *11*, 401–441. https://doi.org/10.1146/annurev.fl.11.010179.002153

Tenreiro, M., Candela, J., Sanz, E. P., Sheinbaum, J., & Ochoa, J. (2018). Near-surface and deep circulation coupling in the western Gulf of Mexico. *Journal of Physical Oceanography*, *48*(1), 145–161. https://doi.org/10.1175/JPO-D-17-0018.1

van Sebille, E., England, M. H., & Froyland, G. (2012). Origin, dynamics and evolution of ocean garbage patches from observed surface drifters. *Environmental Research Letters*, *7*(4), 044040. https://doi.org/10.1088/1748-9326/7/4/044040

Zavala Sansón, L. (2015). Surface dispersion in the Gulf of California. *Progress in Oceanography*, *137*, 24–37. https://doi.org/10.1016/j.pocean.2015.04.008

Zavala Sansón, L., Sheinbaum, J., & Pérez-Brunius, P. (2018). Single-particle statistics in the southern Gulf of Mexico. *Geofísica Internacional*, *57*(2), 139–150. https://doi.org/10.22201/igeof.00167169p.2018.57.2.1693

Zhang, H.-M., Prater, M. D., & Rossby, T. (2001). Isopycnal Lagrangian statistics from the North Atlantic Current RAFOS float observations. *Journal of Geophysical Research*, *106*, 13817–13836. https://doi.org/10.1029/1999JC000101

Zhurbas, V., & Oh, I. (2004). Drifter-derived maps of lateral diffusivity in the Pacific and Atlantic Oceans in relation to surface circulation patterns. *Journal of Geophysical Research*, *109*, C05015. https://doi.org/10.1029/2003JC002241